Radiation of an Aperture Antenna Covered by a Spherical-Shell Chiral Radome and Fed by a Circular Waveguide

Le-Wei Li, *Senior Member, IEEE*, Mook-Seng Leong, *Member, IEEE*, Pang-Shyan Kooi, *Member, IEEE*, Tat-Soon Yeo, *Senior Member, IEEE*, and You-Lin Qiu, *Student Member, IEEE*

***Abstract*—This paper presents a full-wave analysis of the radiation characteristics of an aperture antenna that is flush-mounted on a ground plane and fed by a circular waveguide supporting the dominant TE_{11} mode. The antenna is covered by a dielectric hemispherical chiral radome. Huygen's equivalence principle and the image theory are utilized to simplify the problem. The magnetic dyadic Green's function for the three-layered geometry is formulated and applied to analyze the radiated electromagnetic fields outside the chiral radome. Both the exact and approximate expressions of electric fields valid for the Fresnel and Fraunhofer zones are obtained using the spherical vector wave functions and their approximations in the far zone. Various chiral materials are assumed and computations of antenna parameters are carried out. The effects of the dielectric chiral radome on the radiation power patterns, sidelobe levels, and 3-dB beamwidths are also discussed numerically.**

***Index Terms*— Aperture antennas, chiral media, dielectric radome, dyadic Green's function, electromagnetic wave theory.**

I. Introduction

LAYERED dielectric radomes are frequently required in practice to protect the antenna systems against environmental conditions. The presence of the dielectric radome does, however, affect the radiation characteristics of the antenna system. Therefore, the investigation on what the effects of an dielectric radome are and on how these effects can be minimized has received much attention in the last several decades [1], [2]. For instance, effects of a dielectric radome into which an omnidirectional spiral ultra broad-band antenna was integrated [3], a thin dielectric radome covering a rectangular microstrip antenna array [4], a plane rectangular radome covering an infinite array of microstrip-fed dipoles [5], [6], a large sandwich radome covering an elliptical aperture [7], a dielectric hemisphere covering the slot antennas [8], a spherical-shell radome covering a uniform circular aperture [9], and a hemispherical radome shell with an outer rain-water layer that covers a circular waveguide dominant TE_{11}-mode feed [10] have been investigated.

Manuscript received June 9, 1997; revised December 29, 1997. This work was supported in part by a Grant from the MINDEF/NUS Joint Project 13/96.

The authors are with the Communications and Microwave Division, Department of Electrical Engineering, National University of Singapore, Singapore 119260.

Publisher Item Identifier S 0018-926X(98)03405-X.

To investigate the field (or power) pattern of an antenna covered by a dielectric radome, a variety of methods have been proposed in the literature. The most popular method is the ray tracing technique (RTT) [1], [2], [11]. The (single) plane wave spectrum-surface integral technique [12], [13] as a fast method was also proposed to improve the accuracy of the ray tracing method. The physical optics (PO) method and dielectric physical optics (DPO) technique [14] were developed as well, so as to further increase the computational accuracy. Besides these, the other common techniques such as the moment method (MM) or method of moment (MoM) [14], the variational method, the method of regularization (MoR) [15], the Weigner–Hopf method, the finite-element method (FEM) [16] and dyadic Green's function (DGF) technique have been developed.

In this paper, a full-wave analysis is presented for the radiation characteristics of a realistic circular aperture antenna that is flush-mounted on the ground plane, excited by a circular waveguide supporting the dominant TE_{11} mode, and covered by a spherical-shell chiral radome. To formulate the electromagnetic fields due to such a magnetic surface current, the magnetic type of Green's dyadics are necessarily derived. Following the similar procedure in the literature [9], we proceed as follows.

- The equivalent problem is first derived using the Huygen's principle and image theory.
- The magnetic type of dyadic Green's functions are then formulated and their scattering (including the transmission and reflection) coefficients derived by applying the duality to the electric type of dyadic Green's functions given in [17].
- The rigorous and exact representations of the fields outside the radome are obtained by integrating the function containing the DGF outside the radome and the equivalent magnetic current distribution inside the radome.
- The Fraunhofer electric fields are finally obtained by using the far-zone approximation and by reducing the general formulations.
- The effects of the dielectric radome on the radiation power patterns, sidelobe levels, and 3-dB or half-power beamwidths are finally discussed numerically.

The applicability of the analysis is demonstrated by comparing the results obtained herein with the existing results in the literature.

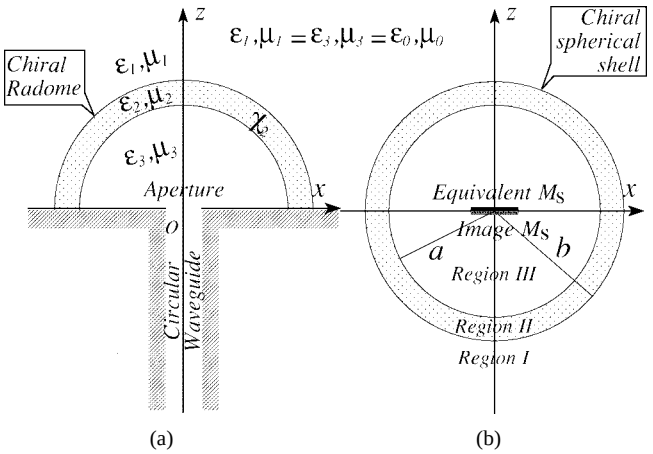

Fig. 1. A circular aperture flush-mounted on an infinite ground plane and covered by a chiral hemispherical shell. (a) An illustration of the geometry. (b) The equivalent problem of the radiation obtained by the use of the image theory.

II. Statement of the Problem

Fig. 1(a) illustrates the geometry of the problem where the aperture is excited by the circular waveguide, mounted on the ground plane, and covered by a chiral hemispherical shell. The waveguide is assumed to support the dominant TE_{11} mode.

In order to obtain the radiated fields, the Huygen's principle together with the image theory is applied. Due to the circular waveguide dominant TE_{11} mode excitation, a magnetic current source $\boldsymbol{M}_s$ over the aperture area can be obtained by applying the Huygen's principle as shown in Fig. 1(b). An image magnetic current source $\boldsymbol{M}_s' = \boldsymbol{M}_s$, shown in Fig. 1(b) below the aperture area, can be assumed by using the image theory. Thus, a problem of radiation from double magnetic current distributions inside a chiral-spherical shell is formed and simplified to the equivalent radiation problem illustrated in Fig. 1(b). Also, the hemispherical radome is equivalent to a spherical shell using the image theory.

A time dependence $\exp(-i\omega t)$ is assumed for the fields throughout the paper. The chiral radome is thus characterized by the following set of constitutive relations:

$$\boldsymbol{D} = \varepsilon_f \boldsymbol{E} + i\chi_f \boldsymbol{H} \tag{1a}$$

$$\boldsymbol{B} = \mu_f \boldsymbol{H} - i\chi_f \boldsymbol{E} \tag{1b}$$

where ε_f, μ_f, and χ_f are the medium's permittivity, permeability, and chirality parameter, respectively, and $f = 1, 2,$ and 3. Therefore, the propagation constant k_f in each layer of the three-layered medium is designated generally as

$$k_f^2 = \omega^2(\mu_f \varepsilon_f - \chi_f^2) \tag{2a}$$

and the symbol ξ_f is defined by

$$\xi_f = \omega\chi_f. \tag{2b}$$

Hence, there are two circularly polarized modes present in the unbounded medium, i.e., the right- and left-handed circularly polarized (RCP and LCP) waves. Their corresponding wave numbers are given by

$$k_f^{(r)} = \xi_f + \omega\sqrt{\mu_f \varepsilon_f} \tag{2c}$$

$$k_f^{(l)} = -\xi_f + \omega\sqrt{\mu_f \varepsilon_f}. \tag{2d}$$

It should be noted that the letters in both bold and italic faces are used to represent the vector operators, while those in bold face only are reserved for the matrices.

Due to the presence of the shell radome, the free-space is divided as shown in Fig. 1(b) into three regions labeled as I, II, and III. The electromagnetic radiation fields $\boldsymbol{E}_f$ and $\boldsymbol{H}_f$ in the fth region ($f = 1, 2,$ and 3) due to the magnetic current distribution $\boldsymbol{M}_s$ located in the third region ($s = 3$ for the innermost region) are expressed in terms of the dyadic Green's function as follows:

$$\boldsymbol{E}_f(\boldsymbol{r}) = -\iiint_V [\nabla \times \overline{\boldsymbol{G}}_m^{(fs)}(\boldsymbol{r}, \boldsymbol{r}') - \xi_f \overline{\boldsymbol{G}}_m^{(fs)}(\boldsymbol{r}, \boldsymbol{r}')] \cdot \boldsymbol{M}_s(\boldsymbol{r}')\, dV' \tag{3a}$$

$$\boldsymbol{H}_f(\boldsymbol{r}) = i\omega\varepsilon_f \iiint_V \overline{\boldsymbol{G}}_m^{(fs)}(\boldsymbol{r}, \boldsymbol{r}') \cdot \boldsymbol{M}_s(\boldsymbol{r}')\, dV' \tag{3b}$$

where the prime denotes the coordinates (r', θ', ϕ') of the magnetic current source $\boldsymbol{M}_s$, V identifies the volume occupied by the source in the third region, and $\overline{\boldsymbol{G}}_m^{(fs)}(\boldsymbol{r}, \boldsymbol{r}')$ denotes the magnetic type of dyadic Green's function. Apparently, the propagation constant in the first and third regions ($f = 1, 3$) of the multilayered achiral medium is designated as $k_f = \omega\sqrt{\mu_f \varepsilon_f}$. By assuming $\xi_f = 0$, the dielectric parameters for chiral media reduce to those for achiral media. Since the two regions are filled with air, thus we have $k_1 = k_3 = k_0$, as shown in Fig. 1.

The field over the aperture shown in Fig. 1 is assumed [18] to be excited by a circular waveguide dominant TE_{11} mode as follows:

$$\begin{aligned}\boldsymbol{E}_a &= E_0\left[\hat{\boldsymbol{\rho}}\frac{J_1(\chi\rho'/r_0)}{\rho'}\sin\phi' + \hat{\boldsymbol{\phi}}\frac{dJ_1(\chi\rho'/r_0)}{d\rho'}\cos\phi'\right]\delta(z') \\ &= E_\rho\hat{\boldsymbol{\rho}} + E_\phi\hat{\boldsymbol{\phi}}\end{aligned} \tag{4}$$

where r_0 is the radius of the circular waveguide feed and the eigenvalue χ and characteristic wave number k_c are given, respectively, by

$$\chi = 1.841 \quad \text{and} \quad k_c = \chi/r_0$$

so that the magnetic current distribution over the aperture can be expressed as

$$\boldsymbol{M}_s = \begin{cases} -2\hat{\boldsymbol{z}} \times \boldsymbol{E}_a, & \rho' \le r_0 \\ 0, & \text{elsewhere.} \end{cases} \tag{5}$$

Using the transformation from the cylindrical coordinates to the spherical coordinates, the magnetic current distribution over the aperture can be expressed in the spherical coordinate system as follows:

$$\begin{aligned}\boldsymbol{M}_s(\boldsymbol{r}') &= 2[E_\phi\hat{\boldsymbol{\rho}} - E_\rho\hat{\boldsymbol{\phi}}] \\ &= 2E_0\left[\hat{\boldsymbol{r}}\frac{dJ_1(\chi r'/r_0)}{dr'}\cos\phi' - \hat{\boldsymbol{\phi}}\frac{J_1(\chi r'/r_0)}{r'}\sin\phi'\right] \\ &\quad \times \frac{\delta\left(\theta' - \frac{\pi}{2}\right)}{r'}.\end{aligned} \tag{6}$$

Apparently, the distribution contains only the first-order term for the eigenvalue m so that the summation with respect to

other eigenvalues ($m \neq 1$) after the integration in either (3a) or (3b) will disappear.

III. Dyadic Green's Function Outside Chiral Radome

A. Representation of Dyadic Green's Function

Under the spherical coordinates, the electromagnetic fields usually consist of the radial-wave modes propagating outwards and inwards. The configuration of the problem is a three-layered geometry (i.e., $N = 3$) and the current source is located in the region III. Hence, the electric dyadic Green's functions for each region $f(= 1, 2$ and $3)$ can be obtained by reducing the generalized dyadic Green's functions for multilayered chiral media formulated by Li *et al.* [17]. Using the duality to the reduced electric dyadic Green's functions, we then obtain the magnetic dyadic Green's functions expressed as follows:

$$\begin{aligned}\overline{\boldsymbol{G}}_{ms}^{(13)}(\boldsymbol{r},\boldsymbol{r}') = {} & \frac{i}{2\pi(k_3^{(r)}+k_3^{(l)})}\sum_{n=0}^{\infty}\sum_{m=0}^{n}(2-\delta_m^0)\frac{2n+1}{n(n+1)} \\ & \times\frac{(n-m)!}{(n+m)!}\Big[\mathcal{C}_{11}^{13}\boldsymbol{V}_{\substack{e\\o}mn}^{(1)}(k_1^{(r)})\boldsymbol{V}'_{\substack{e\\o}mn}(k_3^{(r)}) \\ & +\mathcal{C}_{21}^{13}\boldsymbol{W}_{\substack{e\\o}mn}^{(1)}(k_1^{(l)})\boldsymbol{V}'_{\substack{e\\o}mn}(k_3^{(r)}) \\ & +\mathcal{C}_{13}^{13}\boldsymbol{V}_{\substack{e\\o}mn}^{(1)}(k_1^{(r)})\boldsymbol{W}'_{\substack{e\\o}mn}(k_3^{(l)}) \\ & +\mathcal{C}_{23}^{13}\boldsymbol{W}_{\substack{e\\o}mn}^{(1)}(k_1^{(l)})\boldsymbol{W}'_{\substack{e\\o}mn}(k_3^{(l)})\Big]\end{aligned} \tag{7}$$

and $\mathcal{C}_{11}^{13}$, $\mathcal{C}_{21}^{13}$, $\mathcal{C}_{13}^{13}$, and $\mathcal{C}_{23}^{13}$ are the coefficients of scattering dyadic Green's function to be solved from the boundary conditions.

In (7), the couple of normalized spherical vector wave functions $\boldsymbol{V}_{\substack{e\\o}mn}(k)$ and $\boldsymbol{W}_{\substack{e\\o}mn}(k)$ are orthogonal (as verified by Engheta and Kowarz [19]) among themselves as well as with respect to each other as they are integrated over all the values of r, θ, and ϕ.

B. Transmission Coefficients of Dyadic Green's Function

Following the same procedure of [17] and [20], the coefficients of the scattering dyadic Green's functions are given by

$$\mathcal{C}_{11}^{13} = \frac{(k_3^{(r)})^2\mathcal{T}_{22}^{(1)}}{\mathcal{T}_{11}^{(1)}\mathcal{T}_{22}^{(1)}-\mathcal{T}_{12}^{(1)}\mathcal{T}_{21}^{(1)}} \tag{8a}$$

$$\mathcal{C}_{13}^{13} = -\frac{\mathcal{T}_{12}^{(1)}}{\mathcal{T}_{11}^{(1)}}\mathcal{C}_{23}^{13} \tag{8b}$$

$$\mathcal{C}_{21}^{13} = -\frac{\mathcal{T}_{21}^{(1)}}{\mathcal{T}_{22}^{(1)}}\mathcal{C}_{11}^{13} \tag{8c}$$

$$\mathcal{C}_{23}^{13} = \frac{(k_3^{(l)})^2\mathcal{T}_{11}^{(1)}}{\mathcal{T}_{11}^{(1)}\mathcal{T}_{22}^{(1)}-\mathcal{T}_{12}^{(1)}\mathcal{T}_{21}^{(1)}} \tag{8d}$$

and the elements $\mathcal{T}_{mn}^{(1)}$ are obtainable from

$$\boldsymbol{T}^{(1)} = [\boldsymbol{T}_2][\boldsymbol{T}_1] = [\boldsymbol{\mathcal{F}}_{33}][\boldsymbol{F}_{23}][\boldsymbol{\mathcal{F}}_{23}][\boldsymbol{F}_{13}] \tag{9}$$

where the transmission matrices $\boldsymbol{\mathcal{F}}_{33}$ and $\boldsymbol{\mathcal{F}}_{23}$ in inverse form and $\boldsymbol{F}_{23}$ and $\boldsymbol{F}_{13}$ are defined as

$$\boldsymbol{\mathcal{F}}_{33} = \begin{bmatrix} \partial\hbar_{32}^{(r)} & -\partial\hbar_{32}^{(l)} & \partial\Im_{32}^{(r)} & -\partial\Im_{32}^{(l)} \\ \hbar_{32}^{(r)} & \hbar_{32}^{(l)} & \Im_{32}^{(r)} & \Im_{32}^{(l)} \\ \eta_3\partial\hbar_{32}^{(r)} & \eta_3\partial\hbar_{32}^{(l)} & \eta_3\partial\Im_{32}^{(r)} & \eta_3\partial\Im_{32}^{(l)} \\ \eta_3\hbar_{32}^{(r)} & -\eta_3\hbar_{32}^{(l)} & \eta_3\Im_{32}^{(r)} & -\eta_3\Im_{32}^{(l)} \end{bmatrix}^{-1} \tag{10a}$$

$$\boldsymbol{F}_{23} = \begin{bmatrix} \partial\hbar_{22}^{(r)} & -\partial\hbar_{22}^{(l)} & \partial\Im_{22}^{(r)} & -\partial\Im_{22}^{(l)} \\ \hbar_{22}^{(r)} & \hbar_{22}^{(l)} & \Im_{22}^{(r)} & \Im_{22}^{(l)} \\ \eta_2\partial\hbar_{22}^{(r)} & \eta_2\partial\hbar_{22}^{(l)} & \eta_2\partial\Im_{22}^{(r)} & \eta_2\partial\Im_{22}^{(l)} \\ \eta_2\hbar_{22}^{(r)} & -\eta_2\hbar_{22}^{(l)} & \eta_2\Im_{22}^{(r)} & -\eta_2\Im_{22}^{(l)} \end{bmatrix} \tag{10b}$$

$$\boldsymbol{\mathcal{F}}_{23} = \begin{bmatrix} \partial\hbar_{21}^{(r)} & -\partial\hbar_{21}^{(l)} & \partial\Im_{21}^{(r)} & -\partial\Im_{21}^{(l)} \\ \hbar_{21}^{(r)} & \hbar_{21}^{(l)} & \Im_{21}^{(r)} & \Im_{21}^{(l)} \\ \eta_2\partial\hbar_{21}^{(r)} & \eta_2\partial\hbar_{21}^{(l)} & \eta_2\partial\Im_{21}^{(r)} & \eta_2\partial\Im_{21}^{(l)} \\ \eta_2\hbar_{21}^{(r)} & -\eta_2\hbar_{21}^{(l)} & \eta_2\Im_{21}^{(r)} & -\eta_2\Im_{21}^{(l)} \end{bmatrix}^{-1} \tag{10c}$$

$$\boldsymbol{F}_{13} = \begin{bmatrix} \partial\hbar_{11}^{(r)} & -\partial\hbar_{11}^{(l)} & \partial\Im_{11}^{(r)} & -\partial\Im_{11}^{(l)} \\ \hbar_{11}^{(r)} & \hbar_{11}^{(l)} & \Im_{11}^{(r)} & \Im_{11}^{(l)} \\ \eta_1\partial\hbar_{11}^{(r)} & \eta_1\partial\hbar_{11}^{(l)} & \eta_1\partial\Im_{11}^{(r)} & \eta_1\partial\Im_{11}^{(l)} \\ \eta_1\hbar_{11}^{(r)} & -\eta_1\hbar_{11}^{(l)} & \eta_1\Im_{11}^{(r)} & -\eta_1\Im_{11}^{(l)} \end{bmatrix} \tag{10d}$$

with the following parameters, which are the duality forms of the (29a) and (29b) in [17]:

$$\eta_1 = \sqrt{\frac{\mu_1}{\varepsilon_1}}, \quad \eta_2 = \sqrt{\frac{\mu_2}{\varepsilon_2}}, \quad \eta_3 = \sqrt{\frac{\mu_3}{\varepsilon_3}}. \tag{11}$$

Also, the interparameters for the sake of simplicity are defined as follows:

$$\Im_{im}^{(r,l)} = j_n(k_i^{(r,l)}a_m) \tag{12a}$$

$$\hbar_{im}^{(r,l)} = h_n^{(1)}(k_i^{(r,l)}a_m) \tag{12b}$$

$$\partial\Im_{im}^{(r,l)} = \frac{1}{\rho}\frac{d[\rho j_n(\rho)]}{d\rho}\bigg|_{\rho=k_i^{(r,l)}a_m} \tag{12c}$$

$$\partial\hbar_{im}^{(r,l)} = \frac{1}{\rho}\frac{d[\rho h_n^{(1)}(\rho)]}{d\rho}\bigg|_{\rho=k_i^{(r,l)}a_m}, \tag{12d}$$

$$i = 1, 2, 3; \quad \text{and} \quad m = 1, 2.$$

For the single-layered radome assumed here we have $a_1 = b$ and $a_2 = a$.

IV. Electromagnetic Fields Outside Radome

A. Exact Fields

By making use of the magnetic dyadic Green's function $\overline{\boldsymbol{G}}_m^{(13)}$ in (7), where it is assumed $f = 1$ and $s = 3$, the electric field in the first region outside the radome can be expressed subsequently by

$$\begin{aligned}\boldsymbol{E}_1 = {} & -\iiint_V[\nabla\times\overline{\boldsymbol{G}}_m^{(13)} - \xi_1\overline{\boldsymbol{G}}_m^{(13)}]\cdot\boldsymbol{M}_s\,dV' \\ = {} & -\frac{i2E_0}{k_3^{(r)}+k_3^{(l)}}\sum_{n=1}^{\infty}\frac{2n+1}{n(n+1)}\frac{(n-1)!}{(n+1)!} \\ & \times[(k_1^{(r)}-\xi_1)(\mathcal{C}_{11}^{13}I_{\substack{e\\o}n}+\mathcal{C}_{13}^{13}K_{\substack{e\\o}n})\boldsymbol{V}_{\substack{e\\o}1n}^{(1)}(k_1^{(r)}) \\ & -(k_1^{(l)}+\xi_1)(\mathcal{C}_{21}^{13}I_{\substack{e\\o}n}+\mathcal{C}_{23}^{13}K_{\substack{e\\o}n})\boldsymbol{W}_{\substack{e\\o}1n}^{(1)}(k_1^{(l)})]\end{aligned} \tag{13}$$

where the scattering coefficients $\mathcal{C}^{13}_{11,13,21,23}$ have been given in (8), the vector wave eigenfunctions $\boldsymbol{M}_{\substack{e\\o}1n}(k)$ and $\boldsymbol{N}_{\substack{e\\o}mn}(k)$ can be found from literature [20], [21] and the intermediates $I_{\substack{E\\0}n}$ and $K_{\substack{E\\0}n}$ are expressed as follows:

$$I_{en} = \frac{P_n^1(0)}{\sqrt{2}k_3^{(r)}}\left[n(n+1)\int_0^{r_0}\frac{d[J_1(k_c r')]}{dr'}j_n(k_3^{(r)}r')\,dr' + \int_0^{r_0}J_1(k_c r')\frac{d[r' j_n(k_3^{(r)}r')]}{r'\,dr'}\,dr'\right] \tag{14a}$$

$$I_{on} = \frac{\sqrt{2}}{2}\frac{dP_n^1(\cos\theta)}{d\theta}\bigg|_{\theta=\pi/2}\int_0^{r_0} j_n(k_3^{(r)}r')J_1(k_c r')\,dr' \tag{14b}$$

$$K_{en} = -\frac{P_n^1(0)}{\sqrt{2}k_3^{(l)}}\left[n(n+1)\int_0^{r_0}\frac{d[J_1(k_c r')]}{dr'}j_n(k_3^{(l)}r')\,dr' + \int_0^{r_0}J_1(k_c r')\frac{d[r' j_n(k_3^{(l)}r')]}{r'\,dr'}\,dr'\right] \tag{14c}$$

$$K_{on} = \frac{\sqrt{2}}{2}\frac{dP_n^1(\cos\theta)}{d\theta}\bigg|_{\theta=\pi/2}\int_0^{r_0} j_n(k_3^{(l)}r')J_1(k_c r')\,dr'. \tag{14d}$$

Without loss of any generality, (13) is a *general* expression of the field outside the radome where *all* the regions I, II, and III could be *chiral* media. It is valid for other problems where the same geometry is considered. This result can be further simplified since only the intermediate layer (the radome shell) is chiral medium. In the isotropic spherical layers, only the odd TE modes and even TM modes exist in the electric field distribution. In the presence of the chiral dielectric radome, not only the aforementioned modes, but also the even TE modes and odd TM modes contribute to the electric field outside the spherical shell radome. Also, the electric field has two polar modes: i.e., the RCP and LCP waves.

Also, (13) together with its coefficients in (8) and (14) represents an *exact* expression of the electric field outside the spherical-shell circular radome regardless of the *dimension* of the radome. For its applications such as the radiation characteristics of the aperture antenna excited by the circular waveguide dominant TE_{11} mode, it is desirable to know the electromagnetic fields in the Fraunfoher (far-field) region.

B. Fraunhofer Fields

The expressions given above are the exact solutions of the electric fields valid in the Fresnel zone. The Fraunhofer fields can be further obtained by making use of the far-zone approximation. For the field region in the far zone, we can use the far-field approximation $kr \gg 1$ so that the Hankel function and its derivative can be expressed [22] as follows:

$$h_n^{(1)}(kr) \simeq (-i)^{n+1}\frac{e^{ikr}}{kr} \tag{15a}$$

$$\frac{d[rh_n^{(1)}(kr)]}{kr\,dr} \simeq (-i)^n\frac{e^{ikr}}{kr} \simeq ih_n^{(1)}(kr). \tag{15b}$$

With (15), the far fields can be obtained. To specify the results for our problem stated earlier, we assume that only the intermediate region (i.e., the dielectric radome layer) is made of chiral material. Thus, we have that

$$k_1^{(r)} = k_1^{(l)} = k_0 = \omega\sqrt{\epsilon_0\mu_0} \tag{16a}$$

$$k_2^{(r)} = \xi_2 + \omega\sqrt{\mu_0\epsilon_2} = \xi_2 + k_2 \tag{16b}$$

$$k_2^{(l)} = -\xi_2 + \omega\sqrt{\mu_0\epsilon_2} = -\xi_2 + k_2 \tag{16c}$$

$$k_3^{(r)} = k_3^{(l)} = k_0. \tag{16d}$$

To further discuss the results, we study the field distributions in the two planes, i.e., the $(\phi = (\pi/2))$ plane and the $(\phi = 0)$ plane. In explicit form, the Fraunfoher electric fields in component form can be further expressed as follows.

1) in the $(\phi = (\pi/2)$ plane

$$E_\theta = -\frac{\sqrt{2}E_0}{2k_0}\frac{e^{ik_0 r}}{r}\sum_{n=1}^{\infty}(-i)^n\frac{2n+1}{n^2(n+1)^2} \times\left[iI_{on}(\mathcal{C}^{13}_{11}+\mathcal{C}^{13}_{13}+\mathcal{C}^{13}_{21}+\mathcal{C}^{13}_{23})\frac{dP_n^1(\cos\theta)}{d\theta} - I_{en}(\mathcal{C}^{13}_{11}-\mathcal{C}^{13}_{13}-\mathcal{C}^{13}_{21}+\mathcal{C}^{13}_{23})\frac{P_n^1(\cos\theta)}{\sin\theta}\right] \tag{17a}$$

$$E_\phi = +\frac{\sqrt{2}E_0}{2k_0}\frac{e^{ik_0 r}}{r}\sum_{n=1}^{\infty}(-i)^n\frac{2n+1}{n^2(n+1)^2} \times\left[iI_{en}(\mathcal{C}^{13}_{11}-\mathcal{C}^{13}_{13}+\mathcal{C}^{13}_{21}-\mathcal{C}^{13}_{23})\frac{P_n^1(\cos\theta)}{\sin\theta} + I_{on}(\mathcal{C}^{13}_{11}+\mathcal{C}^{13}_{13}-\mathcal{C}^{13}_{21}-\mathcal{C}^{13}_{23})\frac{dP_n^1(\cos\theta)}{d\theta}\right] \tag{17b}$$

2) in the $(\phi = 0)$-plane

$$E_\theta = -\frac{\sqrt{2}E_0}{2k_0}\frac{e^{ik_0 r}}{r}\sum_{n=1}^{\infty}(-i)^n\frac{2n+1}{n^2(n+1)^2} \times\left[iI_{en}(\mathcal{C}^{13}_{11}-\mathcal{C}^{13}_{13}+\mathcal{C}^{13}_{21}-\mathcal{C}^{13}_{23})\frac{dP_n^1(\cos\theta)}{d\theta} + I_{on}(\mathcal{C}^{13}_{11}+\mathcal{C}^{13}_{13}-\mathcal{C}^{13}_{21}-\mathcal{C}^{13}_{23})\frac{P_n^1(\cos\theta)}{\sin\theta}\right] \tag{18a}$$

$$E_\phi = -\frac{\sqrt{2}E_0}{2k_0}\frac{e^{ik_0 r}}{r}\sum_{n=1}^{\infty}(-i)^n\frac{2n+1}{n^2(n+1)^2} \times\left[iI_{on}(\mathcal{C}^{13}_{11}+\mathcal{C}^{13}_{13}+\mathcal{C}^{13}_{21}+\mathcal{C}^{13}_{23})\frac{P_n^1(\cos\theta)}{\sin\theta} - I_{en}(\mathcal{C}^{13}_{11}-\mathcal{C}^{13}_{13}-\mathcal{C}^{13}_{21}+\mathcal{C}^{13}_{23})\frac{dP_n^1(\cos\theta)}{d\theta}\right] \tag{18b}$$

where

$$I_{en} = \frac{P_n^1(0)}{\sqrt{2}k_0}\left[n(n+1)\int_0^{r_0}\frac{d[J_1(k_c r')]}{dr'}j_n(k_0 r')\,dr' + \int_0^{r_0}J_1(k_c r')\frac{d[r' j_n(k_0 r')]}{r' dr'}\,dr'\right] \tag{19a}$$

$$I_{on} = \frac{dP_n^1(\cos\theta)}{\sqrt{2}\,d\theta}\bigg|_{\theta=\pi/2}\int_0^{r_0} j_n(k_0 r')J_1(k_c r')\,dr'. \tag{19b}$$

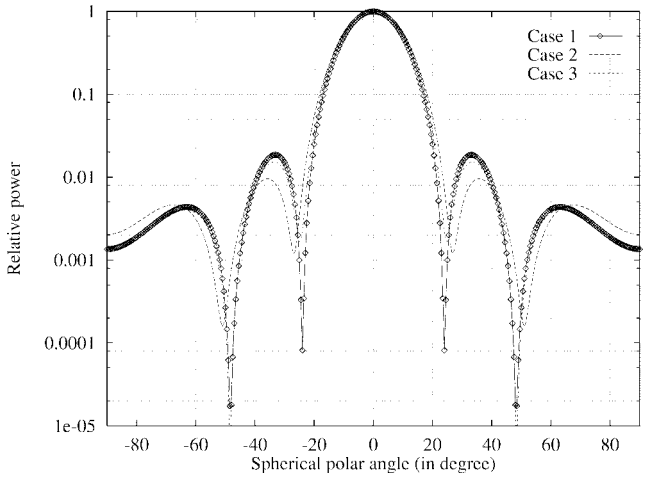

Fig. 2. Power patterns of E_θ in $\phi = (\pi/2)$ plane against spherical polar angle for various chiral parameters. $r_0 = 1.5\lambda_0$ and $\Omega = 0.24, 0.48$ and 0.96.

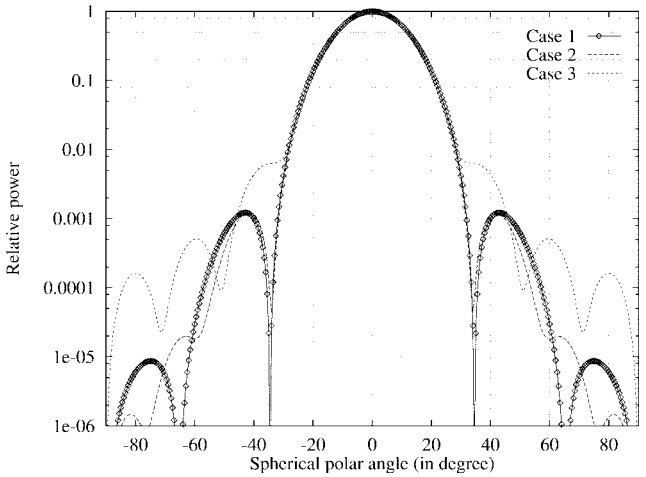

Fig. 3. Power patterns of E_ϕ in $\phi = 0$ plane against spherical polar angle for various chiral parameters, i.e., $\Omega = 0.24, 0.48$ and 0.72. $r_0 = 1.5\lambda_0$.

Obviously, the θ and ϕ components of the electric fields are not the same in both the $(\phi = 0)$ plane and the $(\phi = (\pi/2))$ plane, which indicates that the radially propagating waves are elliptically polarized.

V. Effects of Radome: Numerical Discussions

With the aforegiven formulas of the electromagnetic fields in closed form in the outer region, the numerical evaluation of these fields has been carried out thereafter and the results presented subsequently. Three fundamental quantities, i.e., the antenna pattern, 3-dB beamwidth, and the radiated maximum power, are considered in the numerical computations and the effects of the chirality variation on these quantities are discussed.

A. Antenna Patterns

To show the effects of the chirality on the antenna patterns in the $\phi = (\pi/2)$ and $\phi = 0$ planes, we have computed the power patterns of the aperture antenna (as shown in Figs. 2–5) for various chiral parameter Ω. It is found from the computed results that the half-wave thickness for the dielectric radome should still be assumed as one that bears the least transmission loss. The effects of the radome thickness have been extensively discussed in the literature [9], hence, will not be discussed further.

Fig. 2 (or Fig. 3) shows the $\phi = (\pi/2)$ plane (or $\phi = 0$-plane) power patterns of the antenna due to the contributions from E_θ and E_ϕ against spherical polar angle θ (in degree) for a r_0 of $1.5\lambda_0$ and various chiral parameters Ω corresponding to Cases 1, 2, and 3 (where $\Omega = \xi_c\sqrt{\mu_c/\epsilon_c}$, as in [19]). The inner radius a of the single-layered radome used is 0.5 m or 5 λ_0, the thickness $d = \lambda_e/2$, and the frequency $f = 3$ GHz wherein $\lambda_e = \lambda_0/\sqrt{\epsilon_r}$ for $\epsilon_r = 6.25$.

It is shown previously from the formulation [see (17) and (18)] that only E_θ in $\phi = (\pi/2)$ plane and E_ϕ in $\phi = 0$ plane in the absence of a radome or in the presence of an achiral radome, exist and that both E_θ and E_ϕ in both $\phi = (\pi/2)$ and $\phi = 0$ plane in the presence of a covered chiral radome exist. Quantitively, the E_θ component in the $\phi = (\pi/2)$ plane and E_ϕ component in the $\phi = 0$ plane dominate the field distribution in the far zone. However, the E_ϕ component in the $\phi = (\pi/2)$ plane and E_θ component in the $\phi = 0$ plane change the polarization property of the radiated waves from the previous circular polarization to the current elliptical polarization.

From the comparison, it can also be seen that when the aperture size is small $(r_0 = 1.5\lambda_0)$ as compared with the radome inner dimension ($a = 5\lambda_0$ where the thickness $b - a = \lambda_e/2$), power patterns of E_θ in the $\phi = (\pi/2)$ plane, and E_ϕ in the $\phi = 0$ plane do vary, not even so significantly with chiral parameters (see Fig. 2 and Fig. 3, where the main lobe and sidelobe beamwidths, the sidelobe peak points and null points are changed). However, power patterns of E_ϕ in the $\phi = (\pi/2)$ plane and E_θ in the $\phi = 0$ plane almost do not change with chiral parameters. From the computed results, one more observation is that *the power patterns for* $\Omega = 0$ *and* 0.72 *have very little difference from those for* $\Omega = 0.96$ *and* 0.24. This is why we used different parameters in Fig. 2. This implies that the antenna pattern varies with the chiral parameters perhaps periodically. Details about this phenomenon will be discussed later.

To gain an insight into the effects of multiple reflections and transmissions of the radiated waves, Fig. 4 (or Fig. 5) shows the $\phi = (\pi/2)$ plane (or $\phi = 0$ plane) power patterns of the antenna due to the contributions from E_θ and E_ϕ against spherical polar angle θ (in degree) for a r_0 of $3\lambda_0$ and various chiral parameters Ω corresponding to Cases 2–5 that correspond to $\Omega = 0.24, 0.48, 0.72$, and 0.96. The other parameters utilized here in Figs. 4 and 5 for the aperture and the chiral radome are the same as those used in Figs. 2 and 3. The operating frequency f is 3 GHz. Due to the symmetry, we considered only the positive values of the Ω in this paper although the negative values can also be utilized.

As can be seen from Figs. 4 and 5 (different from those in Figs. 2 and 3) the power patterns of both E_θ and E_ϕ in both $\phi = (\pi/2)$ and $\phi = 0$ planes vary dramatically with the

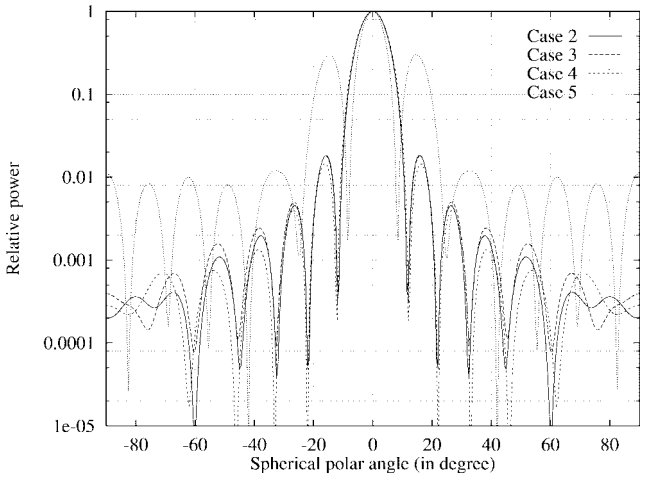

Fig. 4. Power patterns of E_ϕ in $\phi = (\pi/2)$ plane against spherical polar angle for various chiral parameters, i.e., $\Omega = 0.24, 0.48, 0.72$, and 0.96. $r_0 = 3\lambda_0$.

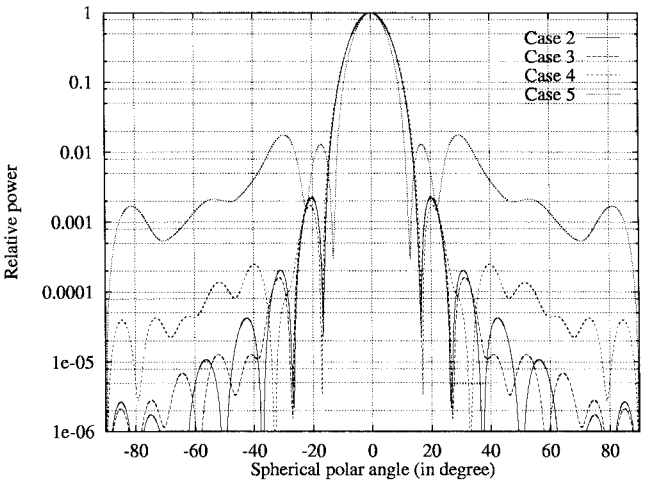

Fig. 5. Power patterns of E_θ in $\phi = 0$ plane against spherical polar angle for various chiral parameters, i.e., $\Omega = 0.24, 0.48, 0.72$, and 0.96. $r_0 = 3\lambda_0$.

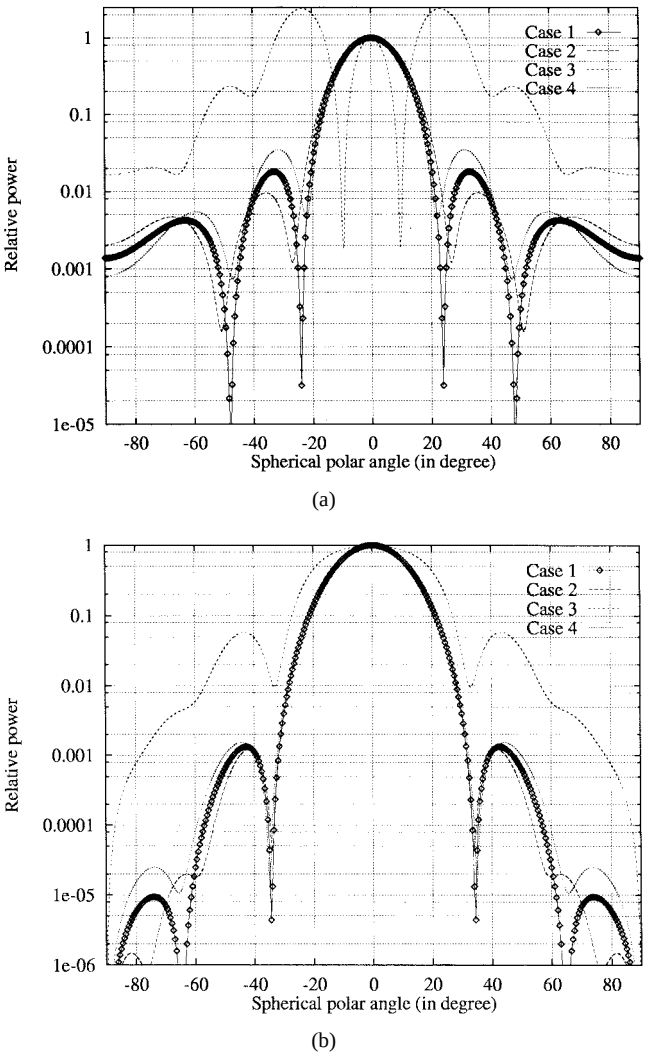

Fig. 6. Power patterns against spherical polar angle for various chiral parameters, i.e., $\Omega = 0, 0.48, 0.49818$, and 0.52. $r_0 = 1.5\lambda_0$. (a) E_θ in $\phi = (\pi/2)$ plane. (b) E_ϕ in $\phi = 0$ plane.

chiral parameter Ω. The 3-dB beamwidths, sidelobe levels, and null points of the patterns change with Ω significantly. The first sidelobes have very high-power level as shown in Fig. 5. Again, it is seen from the results that such variations themselves change periodically.

B. 3-dB Beamwidths

Beamwidth is one of the most important measures of an antenna system. The 3-dB (half-power) beamwidth is an important parameter of an antenna and, hence, is computed for various cases.

From the computation, it is found that the 3-dB beamwidth of both E_θ and E_ϕ components in both $\phi = (\pi/2)$ and $\phi = 0$ planes change very slowly with the chiral parameters. At the points between $\Omega = 0.4$ and $\Omega = 0.6$ there is a kink. This kink is due to the multiple interactions between the chiral radome and the aperture antenna. From the animation of the figures, it is observed that the main lobe of the antenna pattern becomes lower and lower. Instead, the two side lobes near the main lobe increase to a very high level and become the two main lobes between $\Omega = 0.4$ and $\Omega = 0.49818$. With the further increase of the chiral parameter between $\Omega = 0.49818$ and $\Omega = 0.6$, the two sidelobes decreases in power level and the middle lobe becomes higher and higher and returns to the normal case. A periodical variation is observed from the computed results.

To look into the details about the kink, Fig. 6 shows the antenna patterns of E_θ in $\phi = (\pi/2)$ plane and E_ϕ in $\phi = 0$ plane. In Fig. 6, the same aperture and radome dimension parameters as used in Figs. 2 and 3 are assumed except that critical chiral parameters $\Omega = 0$, 0.48, 0.49818 (the peak point of the kink), and 0.52 are used. The absolute values of the respective field components are evaluated and shown in Table I where exactly the same parameters in Fig. 6 are utilized. It is seen from Table I that when $\Omega = 0.49818$ the mode domination of E_θ and E_ϕ is switched over as compared with those modes for achiral case $\Omega = 0$. The mode which dominates the field in $\phi = (\pi/2)$ plane and/or $\phi = 0$ plane has been changed from the E_θ and/or E_ϕ for $\Omega = 0$ to the

TABLE I
ABSOLUTE VALUES OF THE ELECTRIC FIELD POWER COMPONENTS WHEN $\theta = 0^o, r_0 = 1.5\lambda_0$ AND $b - a = \lambda_e/2$

Ω	$\phi = \pi 2$-plane		$\phi = 0$-plane	
	$\lvert E_\theta\rvert^2$	$\lvert E_\phi\rvert^2$	$\lvert E_\theta\rvert^2$	$\lvert E_\phi\rvert^2$
0	1.21647	0	0	1.21647
0.48	0.003737	1.21451	1.21451	0.003737
0.49818	0.0000159	1.21853	1.21853	0.0000159
0.52	0.0062097	1.21273	1.21273	0.0062097

current E_ϕ and/or E_θ for $\Omega = 0.498\,18$. It can also be seen that the polarization still maintains to be circular. In general, the radiated waves are elliptically polarized, as can be seen from Table I for $\Omega = 0.48$ and 0.52. From this analysis, we can see that the polarization of the radiated fields in far zone can be switched between circular and elliptical polarizations.

When the aperture size is comparable with the radome size (e.g., $r_0 = 3\lambda_0$), the multiple interactions between the chiral radome and the aperture antenna is enhanced. Therefore, the values of E_θ and E_ϕ in both $\phi = (\pi/2)$ and $\phi = 0$ planes get closer. However, the variation of the E field components as $r_0 = 3\lambda_0$ is still similar to that as $r_0 = 1.5\lambda_0$. Although the kinks appear in the plotted figures and shifts a bit from the previous $\Omega = 0.498\,18$ to the current $\Omega = 0.490\,33$, the peak point remains almost constant. From the above discussion, it is realized that we can change the 3-dB beamwidth of the power pattern to our desired value for practical design by varying the chiral parameters.

C. Maximum Fields of Main Lobes

As seen previously, the antenna pattern changes in a certain oscillation. Fig. 7 shows how the antenna radiated field components in $\phi = (\pi/2)$- and $\phi = 0$ plane change with the chiral parameters Ω. In the computation, it is assumed that the operating frequency used is $f = 3$ GHz, the inner radius of the chiral radome is $a = 5\lambda_0$ or 0.5 m and the thickness d of the radome is taken as $b - a = \lambda_e/6$, $\lambda_e/4$, $\lambda_e/3$, $2\lambda_e/5$, and $\lambda_e/2$ where $\lambda_e = \lambda_0/\sqrt{\epsilon_r}$.

In the case of $r_0 = 1.5\lambda_0$, Fig. 7 shows the E_θ and E_ϕ components in $\phi = (\pi/2)$ plane (and/or $\phi = 0$-plane) as $\theta = 0^o$ that vary sinusoidally with respect to the parameters Ω. The period of such a sinusoidal oscillation decreases with the chiral radome thickness. It is also seen from the computed results that the $E_\theta^2 + E_\phi^2$ keeps constant with respect to the chiral parameters, demonstrating the energy conservation. Also, it is observed from Fig. 7 that the E_θ (or E_ϕ) varies cosinusoidally (or sinusoidally) with the chiral parameters in $\phi = (\pi/2)$ plane. In $\phi = 0$ plane, the magnitude variations of far-zone E_θ and E_ϕ components are switched over as compared with those components in $\phi = (\pi/2)$ plane.

Clearly, the far-zone E_θ (and/or E_ϕ) component in the $\phi = (\pi/2)$ plane as $\theta = 0^o$ is a cosine (and/or sinusoidal) function of the chiral parameters. On the contrary, the far-zone E_θ (and/or E_ϕ) component in the $\phi = 0$ plane as $\theta = 0^o$ is a sinusoidal (and/or cosine) function.

In the case of $r_0 = 3\lambda_0$, the results resemble those in Fig. 7. However, the magnitude is larger and the period of such sinusoidal variations of $\phi = (\pi/2)$-field components is slightly shorter.

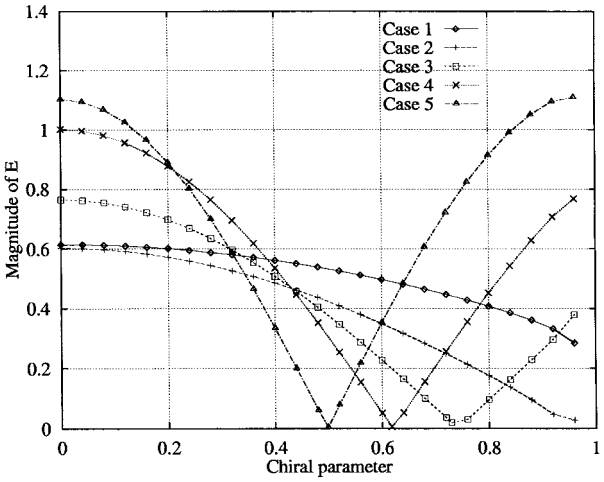

(a)

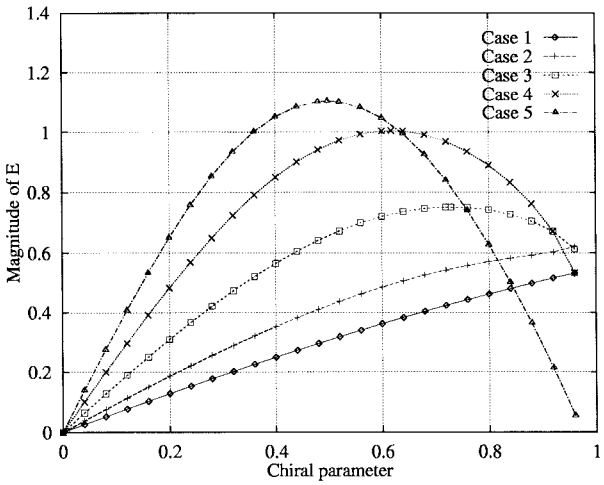

(b)

Fig. 7. Far-zone E_θ and E_ϕ components in $\phi = (\pi/2)$ and $\phi = 0$ planes (for $\theta = 0^o$ and $r_0 = 1.5\lambda_0$) against chiral parameters Ω where for Cases 1–5 the radome thickness $b - a = \lambda_e/6$, $\lambda_e/4$, $\lambda_e/3$, $2\lambda_e/5$, and $\lambda_e/2$. (a) E_θ in $\phi = (\pi/2)$ plane or E_ϕ in $\phi = 0$ plane. (b) E_ϕ in $\phi = (\pi/2)$ plane or E_θ in $\phi = 0$ plane.

VI. CONCLUDING REMARKS

This paper has presented a full-wave analysis of the antenna radiation due to an aperture fed by a circular waveguide TE_{11} wave and covered by a dielectric hemispherical *chiral* radome over the ground plane. First of all, the magnetic DGF's of such a spherically three-layered structure has been formulated and their scattering coefficients derived. The DGF in the outer region is further utilized in the analysis of the electromagnetic fields in the region out of the chiral radome. Exact representation of the field near the chiral radome and far away from the radome have been obtained. Furthermore, the Fraunhofer electric fields have been obtained in closed form using the far-zone approximation. Power patterns in both $\phi = (\pi/2)$ and $\phi = 0$ planes, 3-dB beamwidths of these patterns, and electrical field components at $\theta = 0^o$ have been computed numerically and discussed in detail. As the

dimensions of the antennas and their spherical-shell radomes are electrically large, the equivalent magnetic current method is applicable in the analysis.

From this analysis, the following conclusions can be drawn: 1) due to the chiral radome material the E_θ and E_ϕ components of the electric field exist in both $\phi = (\pi/2)$ and $\phi = 0$ planes. The results reduce automatically to those for the achiral case where E_ϕ component (and E_θ component) in $\phi = (\pi/2)$ plane (and $\phi = 0$ plane) vanishes; 2) aperture antenna power patterns (i.e., the main lobe and sidelobe levels, half-power beamwidths, and null beamwidths) change with the chiral parameter Ω, particularly when the aperture and radome sizes are close. Electromagnetic interaction between the aperture antenna and the radome size increases when their electrical dimensions are comparable; 3) field magnitudes of components E_θ and E_ϕ vary sinusoidally with the chiral parameter Ω; while E_θ increases to a maximum value in both $\phi = (\pi/2)$ and $\phi = 0$ planes, the E_ϕ component drops to a minimum of zero level. This clearly shows the polarization rotation; and 4) the 3-dB (or half-power) beamwidth remains almost constant at the beginning; as the chiral parameter increases a kink arises and, therefore, the 3-dB beamwidth increases suddenly and then drops to a level lower than ever. This implies a possibility that narrower and broader 3-dB beamwidths can be respectively achieved if certain radome material of special chiral parameters is utilized.

ACKNOWLEDGMENT

One of the authors, L.-W. Li, would like to thank Prof. D. L. Jaggard and Prof. N. Engheta, University of Pennsylvania, Philadelphia, PA, and Prof. I. V. Lindell, Helsinki University of Technology, Finland, for their helpful comments and suggestions.

REFERENCES

[1] J. D. Walton Jr., Ed., *Radome Engineering Handbook: Design and Principles.* New York: Marcel Dekker, 1970.
[2] G. A. E. Crone, A. W. Rudge, and G. N. Taylor, "Design and performance of airborne radomes: A review," *Proc. Inst. Elect. Eng.*, vol. 128, pt. F, pp. 451–463, Dec. 1981.
[3] C. Vergnolle, T. Lemoine, and B. Dumont, "Material requirements for microwave antenna into aircraft skins," in *Proc. Smart Structures Mater.—Smart Mater.*, Albuquerque, NM, Feb. 1993, pp. 197–202.
[4] R. Shavit, "Dielectric cover effect on rectangular microstrip antenna array," *IEEE Trans. Antennas Propagat.*, vol. 42, pp. 1180–1184, Aug. 1994.
[5] R.-S. Chu, "Analysis of an infinite phased array of dipole elements with RAM coating on ground plane and covered with dielectric radome," *IEEE Trans. Antennas Propagat.*, vol. 39, pp. 164–176, Feb. 1991.
[6] J. P. R. Bayard, "Analysis of infinite arrays of microstrip-fed dipoles printed on protruding dielectric substrates and covered with a dielectric radome," *IEEE Trans. Antennas Propagat.*, vol. 42, pp. 82–89, Jan. 1994.
[7] R. Shavit, A. P. Smolski, E. Michielssen, and R. Mittra, "Scattering analysis of high performance large sandwich radomes," *IEEE Trans. Antennas Propagat.*, vol. 40, pp. 126–133, Feb. 1992.
[8] A. A. Kishk, G. Zhou, and A. W. Glisson, "Analysis of dielectric-resonator antennas with emphasis on hemispherical structures," *IEEE Antennas Propagat. Mag.*, vol. 36, pp. 20–31, Apr. 1994.
[9] L. W. Li, P. S. Kooi, M. S. Leong, T. S. Yeo, and X. Ma, "An analysis of a circular aperture antenna covered with a dielectric hemispherical shell radome over ground plane," in *Dig. 1995 IEEE AP-S Int. Symp. USNC/URSI Radio Sci. Meet.*, Newport Beach, CA, June 1995, vol. 3, pp. 1442–1445.
[10] M. S. Leong, L. W. Li, P. S. Kooi, T. S. Yeo, and X. Ma, "Layered hemispherical randome analysis including effects of rainfall," in *Proc. Malaysia Int. Conf. Commun. (MICC'95)*, Langkawi Island, Malaysia, Nov. 1995, pp. 12.3.1–12.3.4.
[11] G. A. Deschamps, "Ray techniques in electromagnetics," *Proc. IEEE*, vol. 60, Sept. 1972.
[12] D. C. F. Wu and R. C. Rudduck, "Plane wave spectrum-surface integration technique for radome analysis," *IEEE Trans. Antennas Propagat.*, vol. AP-22, pp. 497–500, May 1974.
[13] D. T. Paris, "Computer aided radome analysis," *IEEE Trans. Antennas Propagat.*, vol. AP-18, pp. 7–15, Jan. 1970.
[14] R. E. Hodges and Y. Rahmat-Samii, "Evaluation of dielectric physical optics in electromagnetic scattering," in *AP-S Int. Symp. Dig.*, Ann Arbor, MI, June 1993, vol. 3, pp. 1742–1745.
[15] A. Y. Svezhentsev, A. I. Nosich, A. Altintas, and T. Oguzer, "Simulation of reflector antenna covered by a circular radome," in *Proc. 9th Int. Conf. Antennas Propagat.*, Eindhoven, The Netherlands, Apr. 1995, pp. 532–535.
[16] R. K. Gordon and R. Mittra, "Finite element analysis of axisymmetric radomes," *IEEE Trans. Antennas Propagat.*, vol. 41, pp. 975–981, July 1993.
[17] L. W. Li, P. S. Kooi, M. S. Leong, and T. S. Yeo, "A general expression of dyadic Green's function in radially multilayered chiral media," *IEEE Trans. Antennas Propagat.*, vol. 43, pp. 232–238, Mar. 1995.
[18] C. A. Balanis, *Antenna Theory: Analysis and Design.* New York: Wiley, 1982.
[19] N. Engheta and M. W. Kowarz, "Antenna radiation in the presence of a chiral sphere," *J. Appl. Phys.*, vol. 67, no. 2, pp. 369–647, 1990.
[20] L. W. Li, P. S. Kooi, M. S. Leong, and T. S. Yeo, "Electromagnetic dyadic Green's function in spherically multilayered media," *IEEE Trans. Microwave Theory Tech.*, vol. 42, , pt. A, pp. 2302–2310, Dec. 1994.
[21] C. T. Tai, *Dyadic Green's Functions in Electromagnetic Theory*, 2nd ed. Piscataway, NJ: IEEE Press, 1994.
[22] J. A. Stratton, *Electromagnetic Theory.* New York: McGraw-Hill, 1941.

Le-Wei Li (S'91–M'92–SM'96), for photograph and biography, see p. 1748 of the December 1997 issue of this TRANSACTIONS.

Mook-Seng Leong (M'81), for photograph and biography, see p. 1748 of the December 1997 issue of this TRANSACTIONS.

Pang-Shyan Kooi (M'75), for photograph and biography, see p. 1748 of the December 1997 issue of this TRANSACTIONS.

Tat-Soon Yeo (M'80-SM'93), for photograph and biography, see p. 1748 of the December 1997 issue of this TRANSACTIONS.

You-Lin Qiu (S'96) received the B.Eng. degree (in electronic engineering) from the Huazhong University of Science and Technology, Wuhan, China, in 1992. She is currently working toward the M.Eng. degree.

Since 1995, she has been with the Electrical Engineering Department of the National University of Singapore as a Research Scholar. From 1992 to 1995 she was a Microwave Engineer at the China Telecommunications, Wuhan, China. Since August 1997 she has been with the Institute of Microelectronics, Singapore (IME) as a Research Engineer. Her current research interests are in the area of microwave radiation and scattering.